A Design Strategy for Vibration Reduction in a Dual-Stator PMSM Based on Combined Mechanical–Electrical Shifting

Young-Jae Kang, Cheon-Ho Song, Byeong-Cheol Bae, Dae-Kee Kim, and Myung-Seop Lim, *Senior Member, IEEE*

***Abstract*— A dual-stator permanent magnet synchronous motor (DS-PMSM) offers both structural and electrical redundancy, making it suitable for high-reliability applications such as urban air mobility (UAM). To address vibration issues that reduce the reliability of propulsion systems, this study proposed a combined mechanical–electrical shifting method that combines mechanical stator shifting with electrical phase adjustment of armature currents. To determine the optimum stator shift angle for effective vibration reduction, the radial air-gap electromagnetic force density (radial AEFD), which is the primary cause of vibration, was analytically derived from the spatial harmonics of the radial air-gap magnetic flux density (AMFD). The variation in AEFD with respect to the stator shift angle and current amplitude was analyzed, and the resulting stator deformation was evaluated using finite-element analysis (FEA). Experimental validation was conducted to verify the stator shift angle that resulted in the minimum deformation and to confirm the trend of deformation variation. The proposed method enables the identification of an optimum stator shift angle that reduces vibration while maintaining torque and efficiency.**

***Index Terms*— Dual stator, electromagnetic force, urban air mobility (UAM), vibration characteristic.**

NOMENCLATURE

p	Number of pole pairs.
Q_s	Number of stator slots.
q	Number of slots per pole per phase.
t	Time.
α	Mechanical angular position.
E	Back-electromotive force.
I	Armature current.
ω	Electrical angular speed.
m	Number of motor phases.
θ_s	Mechanical stator shift angle.
θ_e	Electrical armature current shift angle.
λ	Air-gap relative permeance.
k	Integer multiple index used in slot harmonics.
μ_0	Vacuum permeability.
f_e	Electrical frequency.
F	Magnetomotive force (MMF).
μ	Spatial harmonic order of field MMF.
ν	Spatial harmonic order of armature MMF.
n	Temporal harmonic order of armature MMF.
P_r	Radial air-gap electromagnetic force density (radial AEFD).
P_{amp}	Amplitude of the radial AEFD.
B	Air-gap magnetic flux density (AMFD).
B_r	Radial AMFD.
B_t	Tangential AMFD.
B_{amp}	Amplitude of the radial AMFD.
δ	Phase angle of the MMF.
δ_f	Phase angle of the radial AEFD.
δ_{ro}	Phase angle of the radial AMFD generated by the rotor PM, considering slotting.
$(\cdot)_{ro,os,is}$	Subscripts denoting the rotor, outer stator, and inner stator in the radial components, respectively.

Received 19 May 2025; revised 1 September 2025 and 13 October 2025; accepted 22 October 2025. Date of publication 30 October 2025; date of current version 16 January 2026. This work was supported by the National Research Foundation of Korea (NRF) grant funded by the Korean Government [Ministry of Science and ICT (MSIT)] under Grant RS-2023-00207865. *(Corresponding author: Myung-Seop Lim.)*

Young-Jae Kang, Cheon-Ho Song, and Byeong-Cheol Bae are with the Department of Automotive Engineering (Automotive-Computer Convergence), Hanyang University, Seoul 04763, South Korea (e-mail: dudwo24685@hanyang.ac.kr; chssong@hanyang.ac.kr; byeong@hanyang.ac.kr).

Dae-Kee Kim was with the Department of Automotive Engineering, Hanyang University, Seoul 04763, South Korea. He is currently with Samsung Electronics, Suwon 16677, South Korea (e-mail: haunters@hanyang.ac.kr).

Myung-Seop Lim is with the Department of Automotive Engineering, Hanyang University, Seoul 04763, South Korea (e-mail: myungseop@hanyang.ac.kr).

Digital Object Identifier 10.1109/TTE.2025.3627173

I. INTRODUCTION

RECENTLY, urban air mobility (UAM), including heavy-payload delivery drones and air taxis, has attracted attention in the field of urban transportation [1]. In particular, the electric vertical take-off and landing (eVTOL) propulsion systems used in UAM are considered a fast and eco-friendly alternative in congested urban environments, offering a new approach to urban transportation [2]. As eVTOL systems operate in urban environments, a high level of reliability and safety is required [3].

A dual-stator permanent magnet synchronous motor (DS-PMSM) comprises two separate stators and two inverters that independently control each stator armature winding. This topology provides both mechanical and electrical redundancies, making it suitable for use in eVTOL propulsion systems [4].

UAM platforms, as aircraft, are exposed to continuous vibration [5] and acoustic noise [6]. The primary sources of vibration and acoustic noise in UAM platforms are the eVTOL propulsion systems. Among these, acoustic noise is mainly generated by rotor blades [6], and

2332-7782 © 2025 IEEE. All rights reserved, including rights for text and data mining, and training of artificial intelligence and similar technologies. Personal use is permitted, but republication/redistribution requires IEEE permission.
See https://www.ieee.org/publications/rights/index.html for more information.
Authorized licensed use limited to: Hanyang University. Downloaded on January 23,2026 at 00:17:20 UTC from IEEE Xplore. Restrictions apply.

the contribution of the drive motor to noise is limited. In contrast, the drive motor, which generates mechanical power in eVTOL propulsion systems, is a major source of vibration. Such vibration can lead to failures in power electronics and control systems, posing a serious threat to the overall system reliability and stability [7]. Therefore, the analysis of vibration in drive motors is essential.

Several studies have been conducted to analyze the vibration behaviors of motors. Some studies analyzed the radial electromagnetic force as the primary cause of vibration [8], [9]. Research has shown that radial electromagnetic forces contribute to vibrations, and skewed slots have been proposed to reduce this effect in induction motors [10]. In an interior permanent magnet synchronous motor, a step-skewed rotor has been studied as a method to reduce vibrations [11], and vibration reduction methods employing the response surface method have been proposed [12]. Additionally, research has been conducted on adjusting pole–slot combinations to reduce low-frequency motor vibrations [13]. On the structural side, studies have focused on increasing the mechanical stiffness of the stator [14], [15] and adjusting the stiffness and damping ratios to avoid resonance at specific excitation frequencies [16]. Vibration reduction studies have also been conducted on motor types that have a topology similar to that of a DS-PMSM. In these studies, current phase shifting methods have been applied to reduce vibrations in dual three-phase PMSMs [17], and optimization of winding configurations has been proposed to minimize electromagnetic forces in dual-stator axial flux PMSMs [18]. Research has also been conducted on the electromagnetic forces and vibrations in dual-stator consequent pole hybrid excitation motors [19].

Despite these studies, the research on vibration reduction in the DS-PMSM remains insufficient. In some studies, stator shifting has been attempted to reduce cogging torque in the DS-PMSM [20], [21]. However, those studies did not address vibration analysis. The application of current phase shifting methods, which were developed for the dual three-phase PMSM, to the DS-PMSM has not been reported in previous studies. Moreover, the direct application of current phase shifting can lead to a reduction in torque and efficiency. Therefore, a new approach beyond both conventional shifting methods is required for effective vibration reduction in the DS-PMSM.

In this study, a combined mechanical–electrical shifting method was proposed to address the limitations of both conventional shifting methods in the DS-PMSM. The proposed method is a complementary strategy, in which mechanical stator shifting and current phase shifting are coordinated. The electrical current shift angle is defined in correspondence with the stator shift angle to achieve vibration reduction and torque preservation. To determine the optimum stator shift angle that minimizes vibration, the radial air-gap electromagnetic force density (radial AEFD) was derived analytically, and the resulting stator deformation was analyzed using finite-element analysis (FEA). These results were validated through experimental measurements.

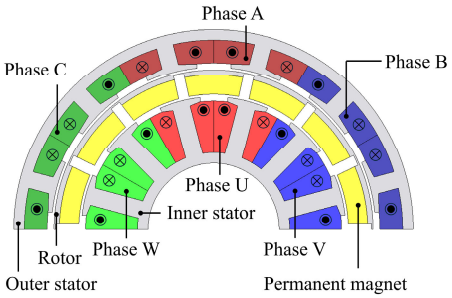

Fig. 1. Configuration of the DS-PMSM.

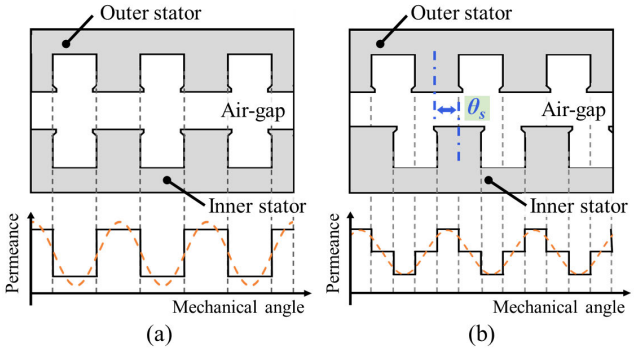

Fig. 2. Comparison of air-gap permeance distribution. (a) Without a stator shift. (b) With stator shift by θ_s.

II. Combined Mechanical–Electrical Shifting Method

In this section, a mechanical–electrical shifting method is proposed to reduce the vibration of the DS-PMSM. The reference model used in this study comprised 14 poles and 12 slots, as illustrated in Fig. 1. This configuration is structurally similar to a surface-mounted permanent magnet synchronous motor, and thus the main drive control strategy is based on the $i_d = 0$ control. Accordingly, the analysis in this study is conducted under the assumption that the influence of the current phase angle, depending on the drive control strategy, is limited.

A. Stator Shifting for Vibration Reduction

The DS-PMSM enables independent control of the amplitude and phase of the armature current in the inner and outer stators. The mechanical angle between the two stators can be adjusted. The mechanical angle and phase difference of the armature currents applied to each stator coil are unique design variables of the DS-PMSM and are defined as follows.

1) Mechanical stator shift angle, θ_s.
2) Electrical current phase shift angle, θ_e.

Both variables influence the performance and vibration characteristics of the DS-PMSM. The mechanical stator shift angle, θ_s, changes the permeance distribution in the air-gap owing to the tooth/slot structure. This change leads to a more sinusoidal air-gap permeance, which improves the vibration characteristics of the DS-PMSM, as shown in Fig. 2.

Authorized licensed use limited to: Hanyang University. Downloaded on January 23,2026 at 00:17:20 UTC from IEEE Xplore. Restrictions apply.

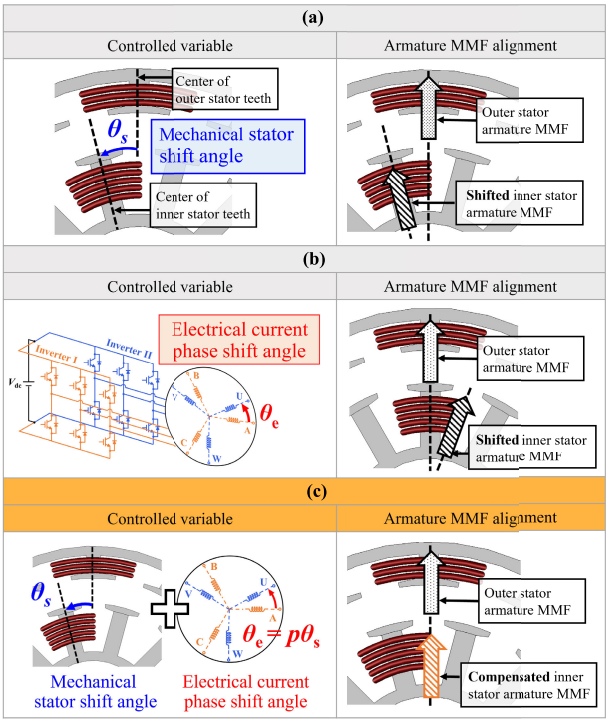

Fig. 3. Comparison of MMF alignment and controlled variables under mechanical shifting, electrical phase shifting, and the proposed method in the DS-PMSM. (a) Stator shifting. (b) Current phase shifting. (c) Proposed method (stator shifting + current phase shifting).

B. Current Phase Shifting for Torque Compensation

Stator shifting can reduce the vibration of the DS-PMSM, but it also results in torque reduction caused by phase misalignment between the magnetomotive forces (MMFs) generated by the inner and outer stator coils. Torque reduction also occurs even without stator shifting, when only the phase of the armature current is shifted, as in conventional methods applied to dual three-phase motors. To compensate for this torque reduction, the proposed method adjusts the electrical phase angle of the armature current θ_e as a function of the stator shift angle θ_s. This relationship is defined by (1) and illustrated in Fig. 3.

$$\theta_e = p\theta_s. \tag{1}$$

The torque generated by the proposed method, in which the inner stator is shifted, is expressed as (2), as shown at the bottom of the page. Here, the subscripts a, b, and c are the three phases of the outer stator windings. The subscripts u, v, and w are the three phases of the inner stator windings. This torque expression represents the phase of the armature current, which is adjusted as defined in (1), to align with the shifted phase of the back-electromotive force caused by stator shifting.

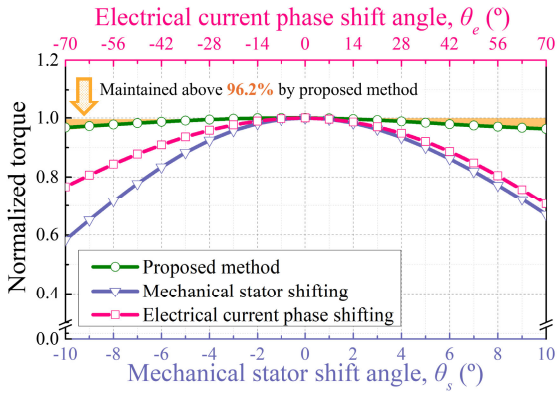

Fig. 4. Comparison of torque performance under mechanical, electrical, and combined shifting.

The effectiveness of the proposed method, which combines mechanical stator shifting and electrical current phase adjustment, was validated through a comparison with each shift strategy. As shown in Fig. 4, when only mechanical stator shifting or current phase shifting is applied, a noticeable torque reduction occurs, depending on the respective shift angle of each strategy. In contrast, although the torque is slightly reduced due to the increased effective air-gap caused by stator shifting, the proposed method maintains the torque above 96.2% across the entire range of the shift angles. These results demonstrate that the proposed method enables more effective torque recovery, achieving up to 38.5 percentage points of improvement compared with the conventional methods, while reducing vibration.

III. Radial AEFD Analysis

To validate the effectiveness of the proposed method, it is essential to analyze the radial AEFD accurately, which is the primary cause of stator vibration. In particular, the vibration order and magnitude of the AEFD are closely related to the stator deformation characteristics and serve as an analytical basis for identifying the optimum stator shift angle. In this section, the AEFD of the DS-PMSM is analyzed under the conditions defined by the proposed method in three steps. First, the dominant vibration orders and excitation frequencies of the AEFD that influence stator deformation are identified. Second, the spatial harmonic components of the radial air-gap magnetic flux density (AMFD) that generate these AEFD components are defined by incorporating the mechanical stator shift angle and electrical current phase shift angle as defined by the proposed method. Finally, the AEFD is derived analytically based on the magnitudes of the AMFD obtained through linear analysis.

$$\begin{aligned} T = {} & \frac{1}{\omega}\left\{E_a\cos(\omega t)I_a\cos(\omega t) + E_b\cos\left(\omega t-\frac{2\pi}{3}\right)I_b\cos\left(\omega t-\frac{2\pi}{3}\right) + E_c\cos\left(\omega t-\frac{4\pi}{3}\right)I_c\cos\left(\omega t-\frac{4\pi}{3}\right)\right\} \\ & + \frac{1}{\omega}\left\{E_u\cos(\omega t-p\theta_s)I_u\cos(\omega t-p\theta_s) + E_v\cos\left(\omega t-\frac{2\pi}{3}-p\theta_s\right)I_v\cos\left(\omega t-\frac{2\pi}{3}-p\theta_s\right)\right. \\ & \left. + E_w\cos\left(\omega t-\frac{4\pi}{3}-p\theta_s\right)I_w\cos\left(\omega t-\frac{4\pi}{3}-p\theta_s\right)\right\} \end{aligned} \tag{2}$$

Authorized licensed use limited to: Hanyang University. Downloaded on January 23,2026 at 00:17:20 UTC from IEEE Xplore. Restrictions apply.

A. Dominant Components of the Radial AEFD

To identify the dominant vibration orders and excitation frequencies of the radial AEFD that influence stator deformation, the radial AEFD P_r is first defined as shown in the following equation:

$$P_r(\alpha,t,\theta_s)=\frac{1}{2\mu_0}\left(B_r^2(\alpha,t,\theta_s)-B_t^2(\alpha,t,\theta_s)\right)\approx\frac{1}{2\mu_0}B_r^2(\alpha,t,\theta_s). \tag{3}$$

Given that the effect of the tangential component is relatively small, this term can be neglected, thus simplifying the expression of P_r. The radial AMFD B_r is expressed in terms of the components of each MMF source, as shown in the following equation:

$$B_r(\alpha,t,\theta_s)=B_{os}(\alpha,t)+B_{ro}(\alpha,t)+B_{is}(\alpha,t,\theta_s)=\begin{pmatrix}F_{os}(\alpha,t)+F_{ro}(\alpha,t)\\+F_{is}(\alpha,t,\theta_s)\end{pmatrix}\lambda(\alpha). \tag{4}$$

The MMFs generated by each source are shown in (5)–(7), and the relative permeance of the outer air-gap is shown in (8)

$$F_{os}(\alpha,t)=\sum_n\sum_\nu F_{os,n\nu}\cos(n\omega t-\nu p\alpha+\delta_{n\nu}) \tag{5}$$

$$F_{is}(\alpha,t,\theta_s)=\sum_n\sum_\nu F_{is,n\nu}\cos\begin{pmatrix}n\omega t-\nu p(\alpha-\theta_s)\\-p\theta_s+\delta_{n\nu}\end{pmatrix} \tag{6}$$

$$F_{ro}(\alpha,t)=\sum_{\mu=2k-1}F_{ro,\mu}\cos\left(\mu\omega t-\mu p\alpha+\delta_\mu\right) \tag{7}$$

where (6) incorporates the stator shift angle θ_s and current phase adjustment $p\theta_s$ defined in the proposed method

$$\lambda(\alpha)=\lambda_0+\sum_k\lambda_k\cos(kQ_s\alpha). \tag{8}$$

Note that the relative permeance in (8) corresponds to the outer air-gap, because the outer stator is the primary analysis target in this study. To derive the radial AEFD, the spatial harmonic order of the armature MMF must be identified first. These harmonic orders, which determine the spatial harmonic components of the radial AMFD, are calculated based on the number of poles and stator slots using the following equations [22]:

$$q=\frac{Q_s}{2\mathrm{pm}}=\frac{z}{c},\quad c\ \&\ z\ \text{are coprime} \tag{9}$$

$$\nu=\begin{cases}\pm\frac{1}{c}(2\mathrm{mj}+1), & c\ \text{is odd}\\ \pm\frac{1}{c}(2\mathrm{mj}+2), & c\ \text{is even}\end{cases} \tag{10}$$

where j is an integer and c and z are the denominator and the numerator, respectively, of the irreducible fraction form of the slots per pole per phase. Based on (9) and (10), the vibration orders and excitation frequencies were predicted for the radial AEFD corresponding to each source and are listed in Table I. For the reference model with 14 poles and 12 slots, the spatial harmonic components of the radial AMFD are determined as $\nu=,\ldots,-17/7,-11/7,-5/7,1/7,1,13/7,19/7,\ldots,$ and $\mu=1,3,5,\ldots,$.

TABLE I

SOURCE, VIBRATION ORDERS, AND FREQUENCIES OF RADIAL AEFD

Source	Vibration order	Frequency
Field	$(\mu_1\pm\mu_2)p$	$(\mu_1\pm\mu_2)f_e$
Armature	$(\nu_1\pm\nu_2)p$	$(n_1\pm n_2)f_e$
Field and armature	$(\mu\pm\nu)p$	$(\mu\pm n)f_e$
Field and stator slotting	$(\mu_1\pm\mu_2)p\pm kQ_s$	$(\mu_1\pm\mu_2)f_e$
Armature and stator slotting	$(\nu_1\pm\nu_2)p\pm kQ_s$	$(n_1\pm n_2)f_e$
Field, armature, and stator slotting	$(\mu\pm\nu)p\pm kQ_s$	$(\mu\pm n)f_e$

TABLE II

PREDICTED SOURCE, VIBRATION ORDERS, AND FREQUENCIES OF RADIAL AEFD WITH SINUSOIDAL CURRENT

Source	Vibration order	Frequency
Field	...-28, -14, 14, 28...	$2f_e$, $4f_e$...
Armature	...-10, -4, 2, 8, 14...	$2f_e$
Field and armature	...-10, -4, -2, 8, 14...	$2f_e$, $4f_e$...
Field and stator slotting	...-12, 2, 12, 16...	$2f_e$, $4f_e$...
Armature and stator slotting	...-10, -4, 2, 14...	$2f_e$
Field, armature, and stator slotting	...-2, 2, 4, 6, 8...	$2f_e$, $4f_e$...

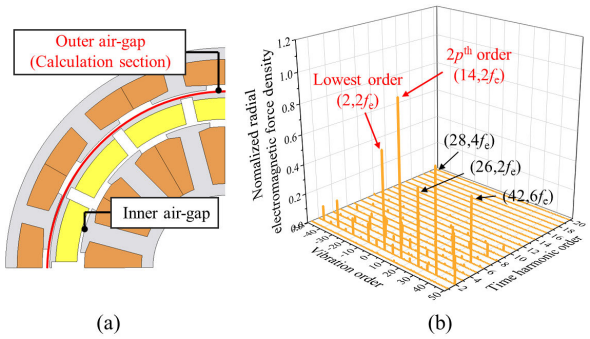

Fig. 5. Spectrum analysis of DS-PMSM. (a) Defined sections for radial AEFD calculation. (b) Spectrum analysis results.

In this study, the current is assumed to be sinusoidal, and the predicted vibration orders and excitation frequencies of the reference model are summarized in Table II. In practice, inverter switching can generate additional temporal harmonics of the current, which are represented by n_1 and n_2 in Table I. The influence of these harmonics can increase if their frequencies approach the natural frequency. In the low-frequency range, where the excitation frequencies are sufficiently apart from the natural frequencies, the vibration response is dominated by the fundamental temporal component of the current. Therefore, the influence of the current harmonics remains limited in this range [23].

Spectrum analysis was performed using FEA to validate the predictions and extract the vibration orders and excitation frequencies of the radial AEFD. The radial AMFD was measured at the outer air-gap, as shown in Fig. 5(a). The results of the spectrum analysis are shown in Fig. 5(b), confirming the analytically predicted vibration orders of the AEFD presented in Table II. The second-order component of the excitation frequencies exhibits the highest amplitude, whereas other components, such as $4f_e$ and $6f_e$, appear with

Authorized licensed use limited to: Hanyang University. Downloaded on January 23,2026 at 00:17:20 UTC from IEEE Xplore. Restrictions apply.

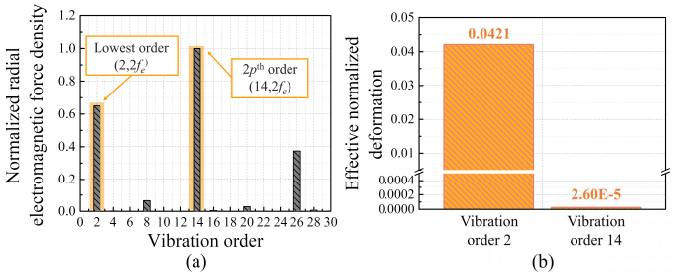

Fig. 6. Comparison of deformation. (a) Vibration order and deformation at twice the fundamental frequency. (b) Normalized deformation of the outer stator.

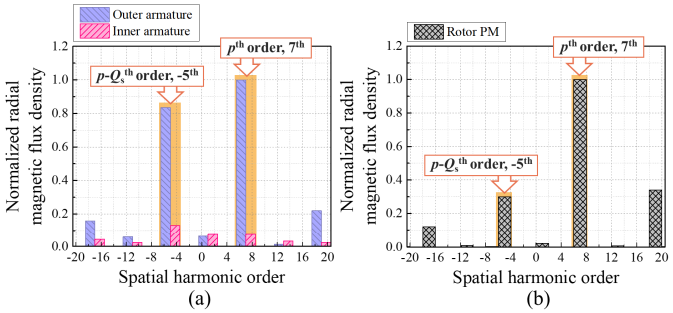

Fig. 7. Spatial harmonics of the radial AMFD based on MMF sources. (a) Radial AMFD of outer and inner armatures. (b) Radial AMFD of rotor PM.

relatively smaller magnitudes. In this study, only the second-order excitation frequency components were considered.

Fig. 6(a) shows the vibration orders at $2f_e$. The 14th vibration order had the largest amplitude, followed by the second vibration order at approximately 67% of the 14th-order amplitude. Despite its lower amplitude, Fig. 6(b) shows that the second vibration order induces a significantly higher deformation of the outer stator than the 14th vibration order. This result is explained by (11), which states that for the same excitation frequency, a lower vibration order leads to higher deformation. Therefore, the vibration analysis in this study focused on the second vibration order

$$Y(v \geq 2) = \frac{12R_{\text{in}}R_{\text{yoke}}^3}{Et_{\text{yoke}}^3\left(r^2-1\right)^2}P_r, \quad (|r| = v) \tag{11}$$

where Y is the static displacement, E is the Young's modulus, R_{in} is the inner radius of the stator, and R_{yoke} is the inner radius up to the yoke.

B. Harmonic Component of the Radial AMFD

Previous studies on fractional-slot concentrated winding PMSM reported that the dominant spatial harmonic components of the radial AMFD are the pole-pair order p and the pole–slot interaction orders $p - Q_s$ [24]. The pole-pair order p originates directly from the fundamental PM field produced. The pole–slot interaction orders $p - Q_s$ originate from the slotting effect, appearing as harmonics produced by the modulation of the fundamental PM field by the slot openings. These two orders exhibit relatively large amplitudes compared with other components. Since the vibration response is mainly influenced by the lower-order spatial harmonics of the radial AMFD, these two orders are adopted as the basis for the analytical model. Fig. 7 presents the amplitudes of the radial AMFD spatial harmonic orders obtained from FEA under the conditions in Table III, which further supports the application of these two orders in the analytical derivation.

C. Derivation and Prediction of Radial AEFD

To derive the second vibration order of the radial AEFD, the radial AMFD generated by each MMF source, considering the slotting effect, is defined in the following equations:

$$B_{os}(\alpha, t) = \sum_{h=p,\ p\text{-}Q_s} B_{os,h}\cos(\omega t - h\alpha) \tag{12}$$

TABLE III
CONFIGURATION OF INDEPENDENTLY ACTIVATED MMF SOURCES

MMF source	B_{os}	B_{ro}	B_{is}
Outer stator armature	ON	OFF	OFF
Rotor PM	OFF	ON	OFF
Inner stator armature	OFF	OFF	ON

$$B_{is}(\alpha, t, \theta_s) = \sum_{h=p,\ p\text{-}Q_s} B_{is,h}\cos\begin{pmatrix}\omega t - h(\alpha-\theta_s)\\ -\ p\theta_s\end{pmatrix} \tag{13}$$

$$B_{ro}(\alpha, t) = \sum_{h=p,\ p\text{-}Q_s} B_{ro,h}\cos(\omega t - h\alpha - \delta_{ro}) \tag{14}$$

where h is the spatial harmonic order considering the slotting effect in the stator. In particular, (13) includes the effect of stator shifting in both the spatial and temporal terms.

The radial AEFD was determined by the interaction between the spatial harmonic components of the radial AMFD generated by each MMF source. For an analytical derivation of the radial AEFD and to simplify the formulation, the total radial AMFD was expressed in terms of its spatial harmonic orders. Thus, using (4) and (12)–(14), the total radial AMFD was decomposed into components for each spatial order, as expressed in the following equation:

$$B_r(\alpha, t, \theta_s) = \sum_{h=p,\ p\text{-}Q_s} B_{r,h}(\alpha, t, \theta_s). \tag{15}$$

The pth-order component of the total radial AMFD is defined in (16), as shown at the bottom of the next page, from the pth-order components generated by each MMF source. The amplitude and the phase angle are given in (17) and (18), as shown at the bottom of the next page, respectively. The $(p - Q_s)$th-order component of the total radial AMFD is defined in (19), as shown at the bottom of the next page. The corresponding amplitude and the phase angle are given in (20) and (21), as shown at the bottom of the next page, respectively. In particular, (19)–(21) are defined as functions of the stator shift angle.

Based on (3) and (15), the $(2p - Q_s)$th vibration order component of the radial AEFD $P_{r,v=2p\text{-}Q_s}$ is derived in (22), as shown at the bottom of the next page, and its amplitude is expressed as a function of the stator shift angle. The conditions for minimizing this amplitude are presented in (23) and (24). The optimum stator shift angle that minimizes the vibration

Authorized licensed use limited to: Hanyang University. Downloaded on January 23,2026 at 00:17:20 UTC from IEEE Xplore. Restrictions apply.

component is determined by (23), while (24) defines the load-dependent phase term ϕ. These conditions can be regarded as a generalized relation. The validity of these conditions is ensured only when the spatial harmonic components $B_{os,p\text{-}Q_s}$ and $B_{ro,p\text{-}Q_s}$ are nonzero. Additionally, a special case occurs when $B_{os,p\text{-}Q_s} = B_{ro,p\text{-}Q_s} \neq 0$ with $\delta_{ro} = \pi \pmod{2\pi}$, which corresponds to perfect cancellation. If both components are zero, the vibration component disappears, and the conditions in (23) and (24) become irrelevant. Although these situations are analytically possible, they are rarely encountered in practical operating conditions

$$\theta_{s,\text{opt}} = \frac{\pi + \phi}{Q_s} + \frac{2\pi k}{Q_s}, \quad k \in \mathbb{Z} \tag{23}$$

$$\phi = \tan^{-1}\left(\frac{B_{ro,p\text{-}Q_s}\sin\delta_{ro}}{B_{os,p\text{-}Q_s} + B_{ro,p\text{-}Q_s}\cos\delta_{ro}}\right). \tag{24}$$

The derived generalized relation indicates that the optimal shift angle for minimizing the radial AEFD is primarily determined by the pole–slot combination. It is also affected by the load condition, which is reflected in the load-dependent phase term ϕ. This term accounts for variations in the magnitude and phase of the radial AMFD. If additional harmonic components exist beyond the two dominant orders considered in this study, the relation can be extended as expressed in the following equations:

$$\theta_{s,\text{opt}} = \frac{\pi + \phi_h}{Q_s} + \frac{2\pi k}{Q_s}, \quad k \in \mathbb{Z} \tag{25}$$

$$\phi_h = \tan^{-1}\left(\frac{\left(B_{ro,p\text{-}Q_s} + \sum_{h\in H} B_{ro,h}\right)\sin\delta_{ro}}{[t]\left(B_{os,p\text{-}Q_s} + \sum_{h\in H} B_{os,h}\right) + \left(B_{ro,p\text{-}Q_s} + \sum_{h\in H} B_{ro,h}\right)\cos\delta_{ro}}\right). \tag{26}$$

To verify the variation in the radial AEFD amplitude with respect to the stator shift angle, a linear analysis was conducted to calculate the magnitude of the radial AMFD, as presented in (12) and (14). A linear analysis was conducted to neglect the effects of saturation at the same location as shown in Fig. 5(a). Fig. 8(a) presents the magnitudes of the radial AMFD generated by the rotor PM and the outer stator armatures, obtained through linear analysis. By substituting these magnitudes into (12) and (14), the amplitude of the $(2p - Q_s)$th vibration order of the radial AEFD expressed in (22) was calculated, and the analytical result is shown in Fig. 8(b). Furthermore, by applying the same AMFD magnitudes to (23) and (24), the calculated optimum stator shift angle was found to coincide with the minimum position in Fig. 8(b).

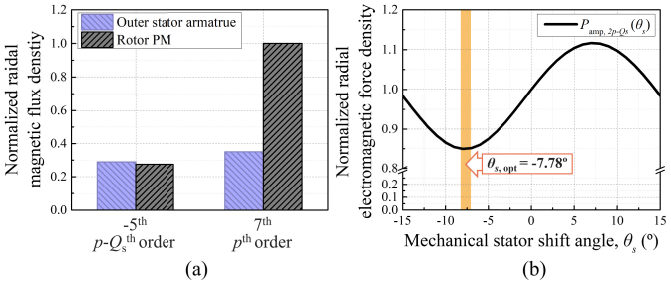

Fig. 8. Derivation of radial AEFD from AMFD harmonics. (a) Magnitudes of the radial AMFD spatial harmonics for each MMF source obtained by linear analysis. (b) Amplitude of the $(2p - Q_s)$th vibration order radial AEFD calculated from (22) as a function of θ_s.

Fig. 9 illustrates the influence of the radial AMFD magnitude on the amplitude of the $(2p - Q_s)$th vibration order of the radial AEFD. This confirms that the waveform of the radial AEFD varies depending on the magnitude of the radial AMFD. In particular, as the magnitude of the radial AMFD decreases, the maximum and minimum positions of the radial AEFD tend to shift to the right.

IV. Stator Deformation Analysis

To determine the optimum stator shift angle that minimizes vibration, this section evaluates the stator deformation of the DS-PMSM through FEA under the conditions defined

$$\begin{aligned} B_{r,p}(\alpha,t,\theta_s) &= B_{os,p}\cos(\omega t - p\alpha) + B_{is,p}\cos(\omega t - p(\alpha-\theta_s) - p\theta_s) + B_{ro,p}\cos(\omega t - p\alpha - \delta_{ro}) \\ &= B_{\text{amp},p}\cos\left(\omega t - p\alpha - \delta_p\right) \end{aligned} \tag{16}$$

$$B_{\text{amp},p} = \sqrt{\left(B_{os,p} + B_{is,p} + B_{ro,p}\cos\delta_{ro}\right)^2 + \left(B_{ro,p}\sin\delta_{ro}\right)^2} \tag{17}$$

$$\delta_p = \tan^{-1}\left(\frac{B_{ro,p}\sin\delta_{ro}}{B_{os,p} + B_{is,p} + B_{ro,p}\cos\delta_{ro}}\right) \tag{18}$$

$$\begin{aligned} B_{r,p\text{-}Q_s}(\alpha,t,\theta_s) &= B_{os,p\text{-}Q_s}\cos(\omega t - (p-Q_s)\alpha) + B_{is,p\text{-}Q_s}\cos(\omega t - (p-Q_s)(\alpha-\theta_s) - p\theta_s) \\ &\quad + B_{ro,p\text{-}Q_s}\cos(\omega t - (p-Q_s)\alpha - \delta_{ro}) \\ &= B_{\text{amp},p\text{-}Q_s}(\theta_s)\cos\left(\omega t - (p-Q_s)\alpha - \delta_{p\text{-}Q_s}(\theta_s)\right) \end{aligned} \tag{19}$$

$$B_{\text{amp},p\text{-}Q_s}(\theta_s) = \sqrt{\left(B_{os,p\text{-}Q_s} + B_{is,p\text{-}Q_s}\cos(Q_s\theta_s) + B_{ro,p\text{-}Q_s}\cos\delta_{ro}\right)^2 + \left(B_{is,p\text{-}Q_s}\sin(Q_s\theta_s) + B_{ro,p\text{-}Q_s}\sin\delta_{ro}\right)^2} \tag{20}$$

$$\delta_{p\text{-}Q_s}(\theta_s) = \tan^{-1}\left(\frac{B_{is,p\text{-}Q_s}\sin(Q_s\theta_s) + B_{ro,p\text{-}Q_s}\sin\delta_{ro}}{B_{os,p\text{-}Q_s} + B_{is,p\text{-}Q_s}\cos(Q_s\theta_s) + B_{ro,p\text{-}Q_s}\cos\delta_{ro}}\right) \tag{21}$$

$$\begin{aligned} P_{r,v=2p\text{-}Q_s}(\alpha,t,\theta_s) &= \frac{1}{2\mu_0}B_{\text{amp},p}\,B_{\text{amp},p\text{-}Q_s}(\theta_s)\cos\left(2\omega t - (2p-Q_s)\alpha - \left(\delta_p + \delta_{p\text{-}Q_s}(\theta_s)\right)\right) \\ &= P_{\text{amp},2p\text{-}Q_s}(\theta_s)\cos\left(2\omega t - (2p-Q_s)\alpha - \delta_f(\theta_s)\right) \end{aligned} \tag{22}$$

Authorized licensed use limited to: Hanyang University. Downloaded on January 23,2026 at 00:17:20 UTC from IEEE Xplore. Restrictions apply.

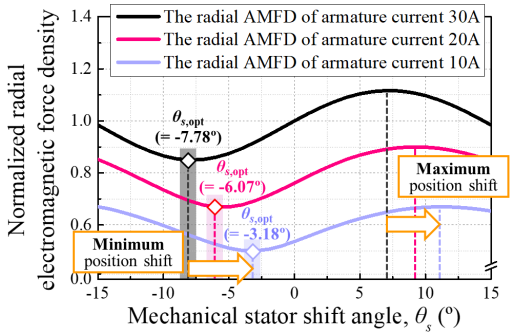

Fig. 9. Waveform shift of the radial AEFD calculated from (22) with respect to the armature radial AMFD magnitude.

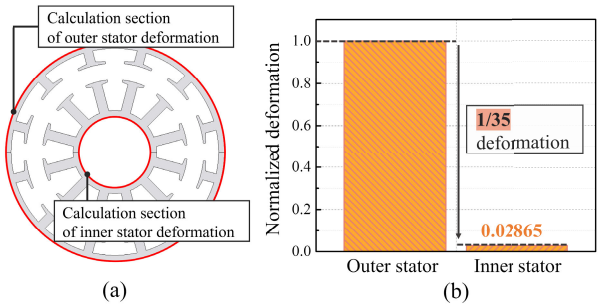

Fig. 10. Comparison of outer and inner stator deformations. (a) Deformation calculation sections. (b) Normalized deformation of each stator.

TABLE IV
MODE SHAPES AND NATURAL FREQUENCIES OF THE OUTER AND INNER STATORS

Stator	2 Mode	3 Mode	4 Mode	5 Mode
Outer	742.8 Hz	2055.6 Hz	3847.1 Hz	6034.5 Hz
Inner	3951.9 Hz	7289.4 Hz	8959.1 Hz	9781.2 Hz

by the proposed method. The influence of the radial AEFD on stator deformation was examined. Specifically, analysis was performed on the AEFD and AMFD generated by each MMF source, at the stator shift angles corresponding to the maximum and minimum deformations. Also investigated were the changes in the positions of the maximum and minimum deformations depending on the current amplitude. Finally, the proposed method was compared with two individual shift strategies in terms of performance and stator deformation. Based on this comparison, the optimum stator shift angle that minimizes vibration while maintaining the performance was identified.

A. Modal Analysis

Modal analysis was used to identify the inherent vibration characteristics of the stator, including its mode shapes and natural frequencies. Because the coils were wound around the stator teeth, an equivalent density that accounted for this effect was considered [20]. Table IV lists the mode shapes and corresponding natural frequencies for both the outer and inner stators. A comparison of the natural frequencies of the two stators revealed that the outer stator exhibited lower natural frequencies than the inner stator.

Because a DS-PMSM comprises both outer and inner stators, it was essential to clearly define the analysis target before conducting a vibration analysis considering stator shifting. In this study, the vibration analysis was conducted under the assumption of a direct-drive configuration without a gearbox. Accordingly, the rotational speed was set to 1000 r/min, which corresponds to the typical blade rotational speed of UAM systems [25]. At this speed, the dominant excitation frequency of the radial AEFD was calculated as 233.3 Hz, which corresponds to twice the electrical frequency. Based on the modal analysis results, the natural frequency of the outer stator (742.8 Hz) was significantly closer to the excitation frequency compared to the inner stator (3951.9 Hz). Consequently, the outer stator is expected to exhibit a significantly higher deformation.

B. Vibration Analysis

To determine the analysis target, vibration analysis was conducted for each stator without stator shifting. The deformation of each stator was evaluated based on the previously obtained modal analysis results and radial electromagnetic forces. The deformation was measured in the section indicated by the red line in Fig. 10(a). The vibration analysis results are shown in Fig. 10(b). The normalized deformation of the outer stator is 1, whereas that of the inner stator is 0.02865, indicating that the deformation of the outer stator is approximately 35 times greater than that of the inner stator. Based on these results, the vibration analysis was focused on the outer stator.

After selecting the analysis target, the effect of shifting the inner stator on the stator deformation characteristics was analyzed. A sinusoidal peak current of 30 A was applied to both the inner and outer stator armatures, and the rotational speed was set to 1000 r/min. The stator shift angle was varied from $-15°$ to $15°$, corresponding to half the stator slot pitch of $30°$. The results of the vibration analysis are presented in Fig. 11. The normalized deformation varies with the inner stator shift angle θ_s, reaching a maximum at $7°$ ($\theta_e = 49°$) and a minimum at $-7°$ ($\theta_e = -49°$). These results indicate that the stator deformation varies with the stator shift angle, which was consistent with the behavior of the radial AEFD.

To investigate the relationship between the stator deformation and vibration order of the radial AEFD, a spectrum analysis of the radial AEFD was conducted at three stator shift angles θ_s: $-7°$ ($\theta_e = -49°$), $7°$ ($\theta_e = 49°$), and $0°$ ($\theta_e = 0°$), corresponding to the minimum deformation position, maximum deformation position, and nonshifting case, respectively. Fig. 12(d) presents the vibration orders of the radial AEFD obtained through FEA. The second vibration order component, previously identified as the dominant contributor to stator deformation, exhibited different amplitudes depending on the

Authorized licensed use limited to: Hanyang University. Downloaded on January 23,2026 at 00:17:20 UTC from IEEE Xplore. Restrictions apply.

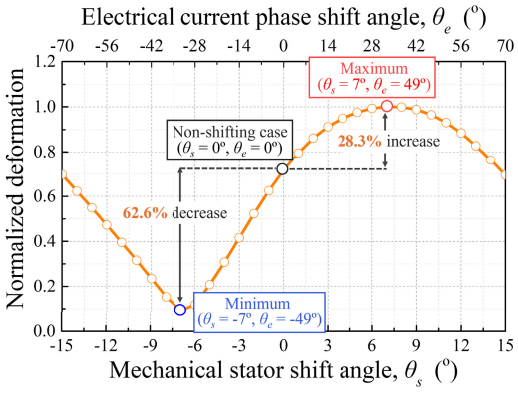

Fig. 11. Outer stator deformation according to the shift angle.

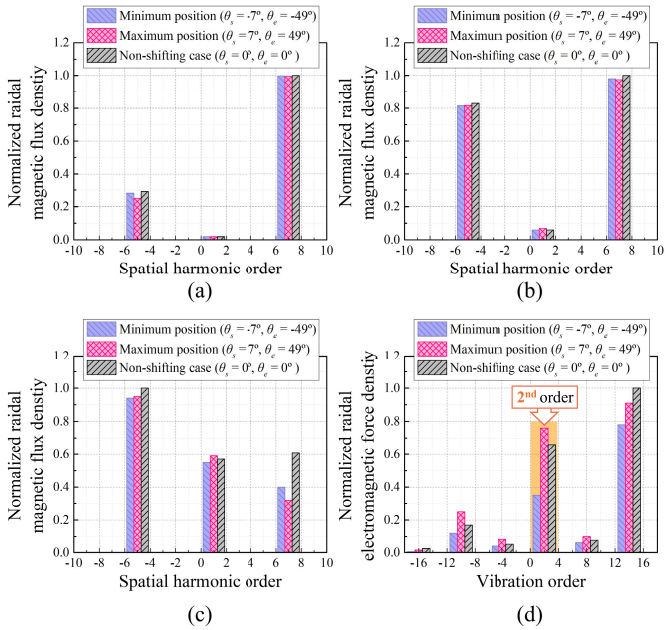

Fig. 12. Spatial harmonics of the radial AMFD and AEFD according to the stator shift angle under the proposed method. (a) Radial AMFD of rotor PM. (b) Radial AMFD of outer armature. (c) Radial AMFD of inner armature. (d) Vibration order of the radial AEFD at $2f_e$.

stator shift angle. These differences correspond to the deformation characteristics, reaching a maximum at 7°, where the stator deformation is also the highest, and a minimum at −7°, where the deformation is the lowest.

To identify whether the AMFD magnitude or stator shift angle has a greater influence on the stator deformation, the spatial harmonics of the radial AMFD generated by each MMF source were analyzed. Fig. 12(a)–(c) presents the radial AMFD results for the rotor PM, outer armature, and inner armature, respectively. In particular, at 7°, where the second vibration order of the radial AEFD component was the most dominant, the radial AMFD magnitudes from all the sources were relatively low. This suggests that the stator deformation is influenced more by the stator shift angle than by the amplitude of the radial AMFD.

In addition, the vibration analysis results for different armature current amplitudes are presented in Fig. 13, which show that the maximum and minimum deformation positions

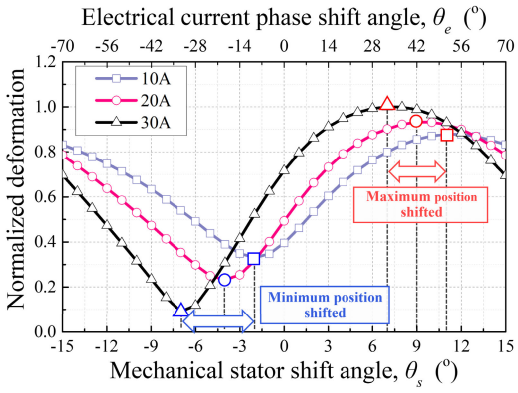

Fig. 13. Deformation of the outer stator according to the shift angle with different current amplitude.

TABLE V
COMPARISON OF EACH SHIFTING STRATEGY AT THE MINIMUM DEFORMATION POSITION RELATIVE TO THE NONSHIFTING CASE

Performance relative to non-shifting case	Stator shifting	Current phase shifting	Proposed method
Maintained Torque	71.00%	79.99%	98.26%
Maintained Efficiency	89.48%	93.84%	99.49%
Reduced radial 2nd AEFD	32.97% ↓	17.06% ↓	52.60% ↓
Reduced stator deformation	38.15% ↓	27.94% ↓	87.55% ↓

shift with the current amplitude. As the current amplitude decreased, both the maximum and minimum deformation positions shifted toward the right. Although a slight difference in the optimal point is observed due to the simplified assumptions and linear analysis condition, the shift tendency of the deformation waveform is consistent with the variation of the analytically derived AEFD waveform with respect to the AMFD magnitude, as illustrated in Fig. 9.

To evaluate the effectiveness of the proposed method, a comparative analysis was conducted of the three shift strategies in terms of performance and stator deformation. Fig. 14 illustrates the FEA results of each method. Fig. 14(a) shows the result of stator shifting, Fig. 14(b) presents the result of current phase shifting, and Fig. 14(c) presents the result of the proposed method. Fig. 14 reveals that the proposed method enables the selection of a shift angle where the deformation is minimized while maintaining performance. In specific cases where a slight performance reduction must be carefully considered, the shift angle can be selected by adjusting the balance between vibration reduction and performance according to design requirements. Even in such cases, the proposed method still achieves more effective vibration reduction compared with the conventional methods.

As summarized in Table V, the proposed method maintains 98.26% of the torque and 99.49% of the efficiency, while reducing the radial second AEFD and the stator deformation by 52.60% and 87.55%, respectively, compared with the nonshifting case. In contrast, other methods exhibit greater losses in torque and efficiency and exhibit less effectiveness in reducing radial AEFD and stator deformation. These results demonstrate that the proposed method effectively reduces vibrations while maintaining high torque and efficiency.

Authorized licensed use limited to: Hanyang University. Downloaded on January 23,2026 at 00:17:20 UTC from IEEE Xplore. Restrictions apply.

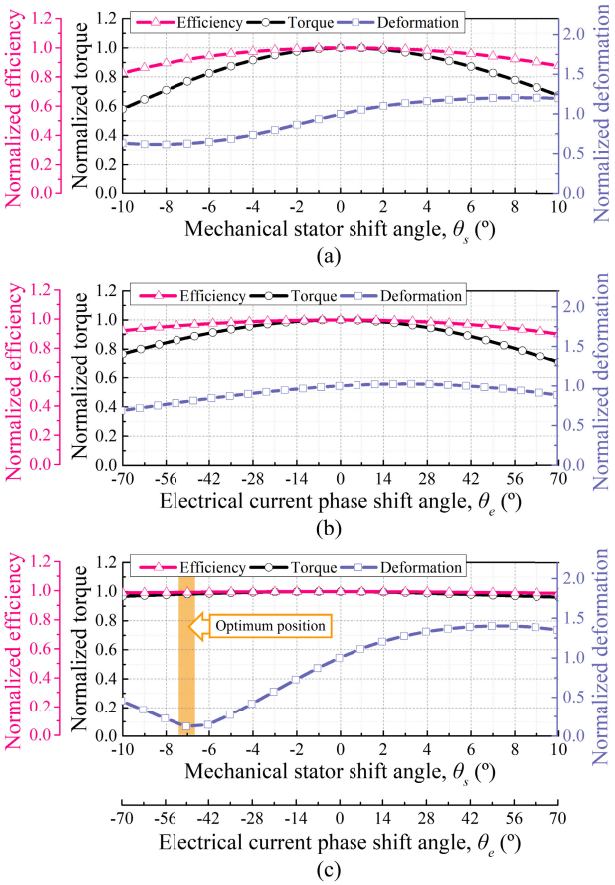

Fig. 14. Comparison of torque, efficiency, and deformation. (a) Stator shifting. (b) Current phase shifting method. (c) Proposed method.

Meanwhile, the proposed method is primarily designed for vibration suppression. Consequently, other performance criteria, such as torque ripple, do not necessarily improve and thus require independent consideration to ensure a balanced assessment of overall performance.

As an additional analysis, the robustness of the proposed method was investigated under varying rotational speeds. In addition to the base condition of 1000 r/min, two additional cases were considered. The first was 7000 r/min, representing a high-speed operating condition in an eVTOL system with a gearbox. The second was 3000 r/min, which is close to the second-mode natural frequency identified in the modal analysis. The corresponding results are shown in Fig. 15. The deformation magnitude varies with speed, with the largest value observed at 3000 r/min due to resonance. Nevertheless, the optimum shift angle remains unchanged for all conditions. This result confirms that the proposed method is robust to variations in operating speed.

V. Verification

This section presents the experimental verification of the vibration characteristics of the DS-PMSM under the conditions defined by the proposed method, focusing on the effects of the inner stator shift angle and input current amplitude. Fig. 16 shows the structure of the DS-PMSM used in the experiment, and Fig. 17 presents the experimental setup for the vibration measurement using accelerometers.

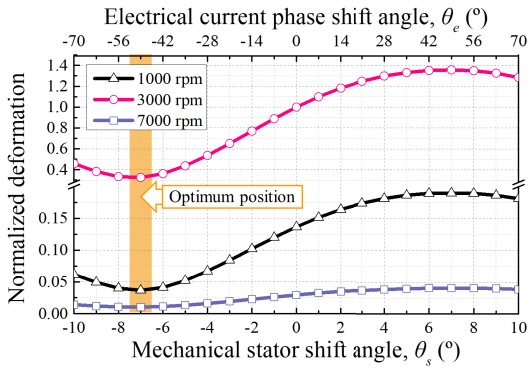

Fig. 15. Comparison of normalized stator deformation at different operating speeds.

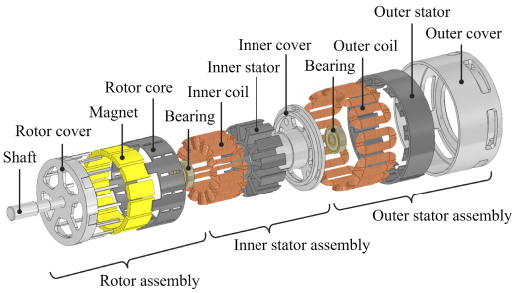

Fig. 16. Structure of the experimental DS-PMSM.

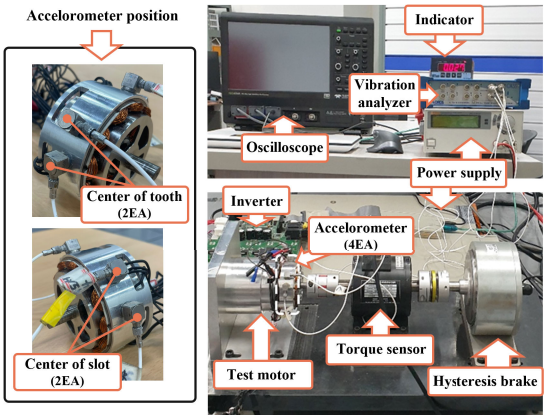

Fig. 17. Experimental setup.

The test motor was connected to a torque sensor and a hysteresis brake, with the voltage and current supplied through a power source and an inverter. To measure the vibration response, four accelerometers (Kistler 8776A50, sensitivity: 100 mV/g, range: ±50 g) were attached to the surface of the outer stator, with two positioned at slot centers and two positioned at tooth centers. Signals were recorded for 5 s using the OROS NVGate data acquisition system. A low-pass filter with a cutoff frequency of 1500 Hz was applied to suppress high-frequency noise and to focus on the dominant excitation component near the excitation frequency. The vibration response was analyzed using the frequency response function to evaluate the stator behavior under radial electromagnetic excitation for each stator shift angle.

The inner stator was shifted in 2° increments in the negative direction, with shift angles of 0°, −2°, −4°, −6°, −8°, and −10°. Fig. 18 illustrates the stator shifting, in which the

Authorized licensed use limited to: Hanyang University. Downloaded on January 23,2026 at 00:17:20 UTC from IEEE Xplore. Restrictions apply.

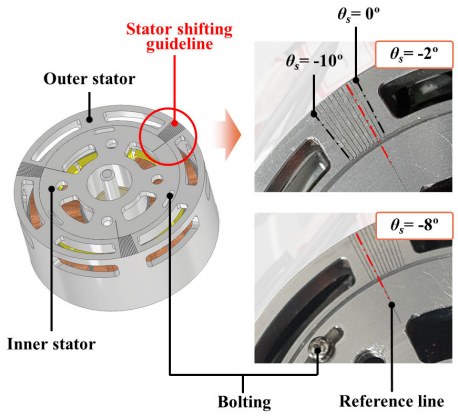

Fig. 18. Stator shifting of the experimental DS-PMSM.

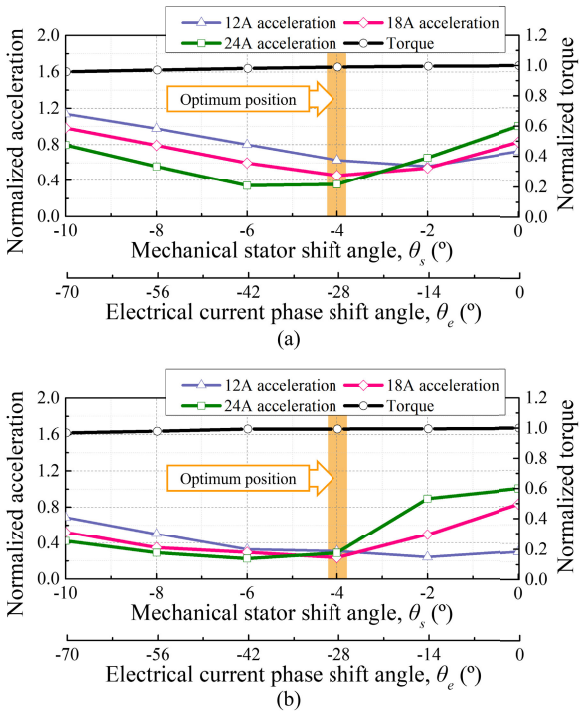

Fig. 19. Normalized acceleration and torque. (a) FEA results. (b) Experimental results.

reference line of the inner stator is aligned with the guideline on the outer stator in the experimental setup. Positive-direction shifting was not feasible owing to a lack of calibration, and precise control of the shift angle was limited, resulting in measurement constraints.

The experiment was conducted at three current amplitudes: 24, 18, and 12 A. The purpose of varying the current was to examine how the positions of the maximum and minimum vibrations changed depending on the operating conditions. Fig. 19(b) shows the measured stator accelerations for each condition. Compared to the FEA results in Fig. 19(a), a similar trend was observed in the increase and decrease in acceleration depending on the inner stator shifting. The minimum vibration positions for each current amplitude consistently matched between the FEA and experimental results. Among these, −4° was identified as the optimal stator shift angle that minimizes vibration across all operating conditions. This confirms the effectiveness of the proposed method in enabling vibration reduction while maintaining torque and efficiency.

VI. Conclusion

This study proposed a combined mechanical–electrical shifting method to minimize the vibration of a DS-PMSM. The proposed method reduces vibration by mechanically shifting the stator and compensates for performance degradation caused by stator shifting through the phase adjustment of the armature currents based on the mechanical stator shift angle. The second vibration order component of the radial AEFD was identified as the dominant factor affecting stator deformation, and its magnitude was analytically derived based on the radial AMFD generated by the rotor permanent magnets and inner and outer stator armatures. The variation in the AEFD magnitude was analyzed with respect to the stator shift angle and the magnitude of the AMFD. In addition, the stator deformation was evaluated through FEA by varying the stator shift angle and current amplitude, and the optimum stator shift angle that minimized the vibration was determined. The identified optimum stator shift angle and the trend of the deformation variation with respect to the stator shift angle were experimentally validated. This study confirms that the proposed method effectively reduces vibration while maintaining torque and efficiency in a DS-PMSM.

References

[1] A. P. Cohen, S. A. Shaheen, and E. M. Farrar, "Urban air mobility: History, ecosystem, market potential, and challenges," *IEEE Trans. Intell. Transp. Syst.*, vol. 22, no. 9, pp. 6074–6087, Sep. 2021.

[2] A. Kasliwal et al., "Role of flying cars in sustainable mobility," *Nature Commun.*, vol. 10, no. 1, Apr. 2019, Art. no. 1555.

[3] A. P. Thurlbeck and Y. Cao, "A mission profile-based reliability modeling framework for fault-tolerant electric propulsion," *IEEE Trans. Ind. Appl.*, vol. 58, no. 2, pp. 2312–2323, Mar. 2022.

[4] S.-W. Hwang, D.-K. Son, S.-H. Park, G.-H. Lee, Y.-D. Yoon, and M.-S. Lim, "Design and analysis of dual stator PMSM with separately controlled dual three-phase winding for eVTOL propulsion," *IEEE Trans. Transport. Electrific.*, vol. 8, no. 4, pp. 4255–4264, Dec. 2022.

[5] S. Gao, F. Shang, and C. Du, "Design of multichannel and multihop low-power wide-area network for aircraft vibration monitoring," *IEEE Trans. Instrum. Meas.*, vol. 68, no. 12, pp. 4887–4895, Dec. 2019.

[6] S. Alam, "Analysis of thrust performance and noise generation of UAM composite propellers fabricated using composite-based additive manufacturing," M.S. thesis, Dept. Mech. Eng., Utah State Univ., Logan, UT, USA, 2025.

[7] F. Rigo, F. Iannuzzo, and G. Meneghesso, "Expected life and failure model in IGBT modules under vibration-induced stress: A case study," *IEEE J. Emerg. Sel. Topics Power Electron.*, vol. 13, no. 1, pp. 945–953, Feb. 2025.

[8] S. Wang, J. Hong, Y. Sun, and H. Cao, "Exciting force and vibration analysis of stator permanent magnet synchronous motors," *IEEE Trans. Magn.*, vol. 54, no. 11, pp. 1–5, Nov. 2018.

[9] I.-S. Jang et al., "Method for analyzing vibrations due to electromagnetic force in electric motors," *IEEE Trans. Magn.*, vol. 50, no. 2, pp. 297–300, Feb. 2014.

[10] D. H. Im, J. H. Chang, S. C. Park, B. I. Kwon, J. P. Hong, and B. T. Kim, "Analysis of radial force as a source of vibration in an induction motor with skewed slots," *IEEE Trans. Magn.*, vol. 33, no. 2, pp. 1650–1653, Mar. 1997.

[11] J.-W. Jung, D.-J. Kim, J.-P. Hong, G.-H. Lee, and S.-M. Jeon, "Experimental verification and effects of step skewed rotor type IPMSM on vibration and noise," *IEEE Trans. Magn.*, vol. 47, no. 10, pp. 3661–3664, Oct. 2011.

[12] J.-W. Jung, S.-H. Lee, G.-H. Lee, J.-P. Hong, D.-H. Lee, and K.-N. Kim, "Reduction design of vibration and noise in IPMSM type integrated starter and generator for HEV," *IEEE Trans. Magn.*, vol. 46, no. 6, pp. 2454–2457, Jun. 2010.

Authorized licensed use limited to: Hanyang University. Downloaded on January 23,2026 at 00:17:20 UTC from IEEE Xplore. Restrictions apply.

[13] D.-Y. Kim, M.-R. Park, J.-H. Sim, and J.-P. Hong, "Advanced method of selecting number of poles and slots for low-frequency vibration reduction of traction motor for elevator," *IEEE/ASME Trans. Mechatronics*, vol. 22, no. 4, pp. 1554–1562, Aug. 2017.

[14] K. Masoudi, M. R. Feyzi, and A. Masoudi, "Reduction of vibration and acoustic noise in the switched reluctance motor by using new improved stator yoke shape," in *Proc. 21st Iranian Conf. Electr. Eng. (ICEE)*, Mashhad, Iran, May 2013, pp. 1–4.

[15] L. Ru, "New stator structure reducing vibration and noise in switched reluctance motor," in *Proc. 18th Int. Conf. Electr. Mach. Syst. (ICEMS)*, Pattaya, Thailand, Oct. 2015, pp. 836–839.

[16] S.-H. Lee, J.-P. Hong, S.-M. Hwang, W.-T. Lee, J.-Y. Lee, and Y.-K. Kim, "Optimal design for noise reduction in interior permanent-magnet motor," *IEEE Trans. Ind. Appl.*, vol. 45, no. 6, pp. 1954–1960, Nov. 2009.

[17] S. Zhu, W. Zhao, G. Liu, Y. Mao, and Y. Sun, "Effect of phase shift angle on radial force and vibration behavior in dual three-phase PMSM," *IEEE Trans. Ind. Electron.*, vol. 68, no. 4, pp. 2988–2998, Apr. 2021.

[18] Y. Lu, J. Li, R. Qu, D. Ye, and H. Lu, "Electromagnetic force and vibration study on axial flux permanent magnet synchronous machines with dual three-phase windings," *IEEE Trans. Ind. Electron.*, vol. 67, no. 1, pp. 115–125, Jan. 2020.

[19] Z. Wu, Y. Fan, H. Chen, X. Wang, and C. H. T. Lee, "Electromagnetic force and vibration study of dual-stator consequent-pole hybrid excitation motor for electric vehicles," *IEEE Trans. Veh. Technol.*, vol. 70, no. 5, pp. 4377–4388, May 2021.

[20] W. Gul, Q. Gao, A. Walker, T. Zou, H. Huang, and C. Gerada, "Mitigation of cogging torque in a double-stator single-rotor PMSG for direct drive offshore wind turbines," in *Proc. IEEE Int. Electr. Mach. Drives Conf. (IEMDC)*, San Francisco, CA, USA, May 2023, pp. 1–6.

[21] G.-C. Lee and T.-U. Jung, "Cogging torque reduction design of dual stator radial flux permanent magnet generator for small wind turbine," in *Proc. IEEE Tencon Spring*, Sydney, NSW, Australia, Apr. 2013, pp. 85–89.

[22] J. F. Gieras, C. Wang, and J. C. Lai, *Noise Polyphase Electric Motors*. Boca Raton, FL, USA: CRC Press, 2006.

[23] F. Lin, S. Zuo, W. Deng, and S. Wu, "Modeling and analysis of electromagnetic force, vibration, and noise in permanent-magnet synchronous motor considering current harmonics," *IEEE Trans. Ind. Electron.*, vol. 63, no. 12, pp. 7455–7466, Dec. 2016.

[24] J.-H. Kim, Y.-J. Won, and M.-S. Lim, "Analysis and reduction of radial vibration of FSCW PMSM considering the phase of radial, tangential forces, and tooth modulation effect," *IEEE Trans. Transport. Electrific.*, vol. 11, no. 1, pp. 2976–2987, Feb. 2025.

[25] T. F. Tallerico, J. Chapman, and A. D. Smith, "Preliminary electric motor drivetrain optimization studies for urban air mobility vehicles," in *Proc. IEEE/AIAA Transp. Electrific. Conf. Electr. Aircr. Technol. Symp. (ITEC+EATS)*. Anaheim, CA, USA: NASA Glenn Research Center, Jun. 2022

Young-Jae Kang received the bachelor's degree in automotive engineering from Hanyang University, Seoul, South Korea, in 2024, where he is currently pursuing the Ph.D. degree in automotive engineering.

His research interests include the design and optimization of electric machines and the analysis of electromagnetic fields.

Cheon-Ho Song received the bachelor's and master's degrees in electrical engineering from Hanbat National University, Daejeon, South Korea, in 2019 and 2021, respectively. He is currently pursuing the Ph.D. degree in automotive engineering with Hanyang University, Seoul, South Korea.

His research interests include the design and analysis of electric machines for electromechanical systems.

Byeong-Cheol Bae received the bachelor's degree in automotive engineering from Hanyang University, Seoul, South Korea, in 2023, where he is currently pursuing the Ph.D. degree in automotive engineering.

His research interests include the design and optimization of electric machines and the analysis of electromagnetic fields.

Dae-Kee Kim received the bachelor's degree in mechanical engineering and the Ph.D. degree in automotive engineering from Hanyang University, Seoul, South Korea, in 2014 and 2022, respectively.

He has been with Samsung Electronics, Suwon, South Korea, as a Staff Engineer since 2022. His research interests include noise and vibration analysis of electric machinery for domestic appliances.

Myung-Seop Lim (Senior Member, IEEE) received the bachelor's degree in mechanical engineering and the master's and Ph.D. degrees in automotive engineering from Hanyang University, Seoul, South Korea, in 2012, 2014, and 2017, respectively.

From 2017 to 2018, he was a Research Engineer with Hyundai Mobis, Yongin, South Korea. From 2018 to 2019, he was an Assistant Professor with Yeungnam University, Daegu, South Korea. Since 2019, he has been with Hanyang University, where he is currently an Associate Professor. His research interests include electromagnetic field analysis and multiphysics analysis of electric machinery for mechatronics systems, such as automotive and robot applications.

Authorized licensed use limited to: Hanyang University. Downloaded on January 23,2026 at 00:17:20 UTC from IEEE Xplore. Restrictions apply.